Bulletin of the Seismological Society of America, Vol. 81, No. 5, pp. 1573–1602, October 1991

RUPTURE HISTORY OF THE 1989 LOMA PRIETA, CALIFORNIA, EARTHQUAKE

BY JAMISON H. STEIDL, RALPH J. ARCHULETA, AND STEPHEN H. HARTZELL

ABSTRACT

Strong motion records of the 1989 Loma Prieta earthquake are inverted to determine a model of the rupture history. Uncorrected horizontal and vertical accelerograms are integrated to particle velocity time histories for 38 stations within an epicentral range of 75 km. The time histories are bandpassed filtered with corners at 0.05 and 1.0 Hz. These bandpassed time histories are inverted using a nonlinear method to solve for the distribution of slip amplitudes and rupture times at specified locations on the fault plane. The fault plane is specified *a priori*: 38 km long and 17 km wide, extending from 3 to 19 km depth at a constant dip of 70°. Starting models have rupture times based on constant rupture velocities of 2.5, 2.8, and 3.0 km/sec and uniform slip with rise times of 0.5, 1.0, 1.5, and 3.0 sec.

The waveform inversion results show the strike-slip displacement is concentrated at the southern end of the rupture (rake = 156°) and the dip-slip displacement is concentrated at the northern end of the rupture (rake = 115°). The average total slip is partitioned almost equally between strike slip and dip slip (rake = 137°). The hypocentral area has an unusually small amount of slip with almost no slip in a region just to the north and up dip from the hypocenter. The rupture front is complex, propagating up dip to the south faster than it propagates to the north. The region of maximum strike slip to the southeast radiates simultaneously with the region of maximum dip slip to the northwest. The average rupture velocity is 3.0 km/sec, approximately 0.83 times the local shear wave speed. The calculated seismic moment is $3.5 \pm 0.5 \times 10^{26}$ dyne-cm.

INTRODUCTION

The $M_s = 7.1$, 18 October 1989, Loma Prieta earthquake (origin time: 00h, 04mn, 15.2 sec GMT, epicenter 37.04°N, 121.88°W) provided one of the most complete sets of near-source strong motion records ever. The azimuthal distribution of strong motion instruments in the vicinity of the Loma Prieta event provides strong constraints on determining dynamic rupture propagation and slip amplitudes. This study uses these data to determine details of the rupture history by waveform inversion.

The Loma Prieta earthquake ruptured a part of the San Andreas fault, which was thought to have previously ruptured during the 1906 San Francisco event (Scholz, 1985). The slip measured at the surface associated with the 1906 event has been broken into two distinct sections: a northern section with a 4.0-m offset and a southern section with a 1.0-m offset. Although the 1906 surface measurements in the Loma Prieta segment are questionable, this southern section is thought to have been an area of slip deficit that would eventually rupture, catching up with the slip on the northern section (Scholz, 1985). It is this southern region that produced the Loma Prieta event. Does this mean the slip on the southern section has now caught up to the northern section? Determination of the distribution of slip is essential in trying to answer this question.

Modeling of earthquake rupture processes at spatial resolutions on the order of 1.0 to 2.0 km and temporal resolutions on the order of 0.5 to 2.0 sec has demonstrated complex spatial distributions of slip and variations in rupture velocity for most earthquakes (e.g., Aki, 1968; Heaton and Helmberger, 1979; Archuleta and Day, 1980; Bouchon, 1982; Olson and Apsel, 1982; Hartzell and Heaton, 1983; Archuleta, 1984; Beroza and Spudich, 1988; Hartzell, 1989; Mendoza and Hartzell, 1989; Hartzell and Iida, 1990; Hartzell and Mendoza, 1991). Stresses are relieved in regions of large slip and increased in areas where little or no slip occurs. Determination of the slip distribution is important, because it is this distribution of static slip that sets the stage for future events. Regions of high slip would have a lower probability of producing another event in the near future. Because the rupture failed to reach the surface in the Loma Prieta earthquake, there are no direct measurements of the slip. Of course, the actual evolution of the faulting process is not directly observable. Thus determination of slip amplitudes and distribution, plus the details of rupture propagation, depends on geophysical techniques such as that used in this study.

Data

The strong motion data used in this study consist of horizontal and vertical accelerograms recorded at 38 stations within a 75-km epicentral distance (Table 1), operated by the California Division of Mines and Geology (CDMG) and the United States Geological Survey (USGS). The distribution of stations is shown in Figure 1. Initially, all of these stations were used; however, in later inversions some stations were deleted because of strong site effects. With increasing epicentral distance, the misfit in phase information due to differences between the actual and assumed velocity structure becomes more critical. Thus the number of distant stations was also reduced in later inversions (Fig. 4).

Each station recorded three components of ground acceleration, making a total of 114 records in the data set. Initially, we used only the horizontal components (76 records) in the inversions, so that the numerical problem could be contained within 32 megabytes of RAM memory of our SUN 4/470 minicomputer, keeping computation time to a minimum (about 125 CPU hours per model). We included the vertical component records in later inversions when the number of stations was reduced.

Because of the difficulty in modeling high frequencies, the uncorrected acceleration records were integrated to particle velocity. The data were then band-passed filtered with corners at 0.05 and 1.0 Hz to allow for a direct comparison between data and synthetics in the same bandwidth. Only the first 35.0 sec of each record was inverted. Later this time window was decreased to 20.0 sec for some inversions.

Method

A fault plane striking 126° and dipping 70° was divided into equal area subfaults (Fig. 2). The fault plane has a length of 38 km and a down-dip width of 17 km, extending from a depth of 3 to 19 km. The allowable rupture area comprises 152 subfaults, each 2 by 2.125 km. The hypocenter is located at the midway point along strike at a depth of 18 km (Langston *et al.*, 1990; USGS Staff, 1990). The velocity model is identical to that used by the USGS to locate aftershocks in this region. The USGS model consists of 2 one-dimensional

TABLE 1

STRONG MOTION STATIONS

Station	Latitude	Longitude	Epicentral Distance (km)	Owner	Components
COR Coralitos*†	37.046	121.083	5	CDMG	90°, 0°
WAT Watsonville†	36.909	121.756	20	CDMG	90°, 0°
CAP Capitola*	36.974	121.952	10	CDMG	90°, 0°
UCS U.C. Santa Cruz*	37.011	122.060	15	CDMG	90°, 0°
GOF Gilroy-Old Firehouse§	37.009	121.569	30	CDMG	180°, 90°
GGC Gilroy-Gavilan College*	36.973	121.568	30	CDMG	67°, 337°
GI1 Gilory #1†	36.973	121.572	30	CDMG	90°, 0°
GI2 Gilroy #2†	36.982	121.556	30	CDMG	90°, 0°
GI3 Gilroy #3†	36.987	121.536	30	CDMG	90°, 0°
GI4 Gilroy #4†	37.005	121.522	30	CDMG	90°, 0°
GI6 Gilroy #6*†	37.026	121.484	35	CDMG	90°, 0°
GI7 Gilroy #7*	37.033	121.434	40	CDMG	90°, 0°
SAR Saratoga*	37.255	122.031	30	CDMG	90°, 0°
HOL Hollister (South and Pine)†	36.848	121.397	50	CDMG	90°, 0°
ASH Agnews State Hospital†	37.397	121.952	45	CDMG	90°, 0°
FRS Foster City-Redwood Shores†	37.55	122.23	70	CDMG	90°, 0°
ADL Anderson Dam-Abutment*	37.166	121.628	30	USGS	340°, 250°
ADD Anderson Dam-Downstream*†	37.166	121.628	30	USGS	340°, 250°
SUN Sunnyvale†	37.402	122.024	45	USGS	0°, 270°
HOA Hollister Airport†	36.888	121.413	45	USGS	255°, 165°
PAH Palo Alto VA Hospital	37.40	122.14	50	USGS	302°, 212°
SLA Stanford-SLAC†	37.419	122.205	50	USGS	0, 270°
HCH Hollister City Hall†	36.851	121.402	50	USGS	0, 270°
SPG Stanford-parking garage	37.431	122.171	50	USGS	0, 270°
MPH Menlo Park VA Hospital	37.468	122.157	55	USGS	110°, 20°
FRE Freemont-Emerson Court*	37.535	121.929	55	USGS	180°, 90°
RED Redwood City-APEEL stn. #2	37.52	122.25	65	USGS	133°, 43°
LEX Lexington Dam-Abutment†	37.202	121.949	20	CDMG	90°, 0°
CLD Coyote Lake Dam-Downstream*†	37.118	121.550	30	CDMG	195°, 105°
CLA Coyote Lake Dam-Abutment†	37.124	121.551	30	CDMG	195°, 105°
HVL Halls Valley-Grant Park*†	37.338	121.714	35	CDMG	90°, 0°
SAG SAGO South-Hollister*†	36.753	121.396	50	CDMG	261°, 171°
SAL Salinas*†	36.671	121.642	45	CDMG	160°, 70°
MCH Monterey City Hall*†	36.597	121.897	50	CDMG	90°, 0°
WFS Woodside Fire Station*	37.429	122.258	55	CDMG	90°, 0°
CSS Crystal Springs Res.-Skyline*	37.465	122.323	65	CDMG	90°, 0°
CSP Crystall Springs Res.-Pulgas*†	37.49	122.31	65	CDMG	90°, 0°
FMS Freemont-Mission San Jose*†	37.530	121.919	55	CDMG	90°, 0°

* 20 stations used in second set of inversions.

† Stations with absolute time.

vertical models, separated at the trace of the San Andreas. One model corresponds to the Franciscan geology to the northeast and the other to the Salinian geology to the southwest. The northeast velocity model is used in this study (Table 2), because a larger percentage of the stations are located on the northeast side of the San Andreas fault. Future work may include separate Green's functions to account for azimuthal variations in the velocity model.

Complete synthetics, including body waves, surface waves, and leaky modes, have been generated for every subfault in the frequency range 0.0 to 1.5 Hz using discrete wavenumber/finite element (DWFE) Green's functions (Olson

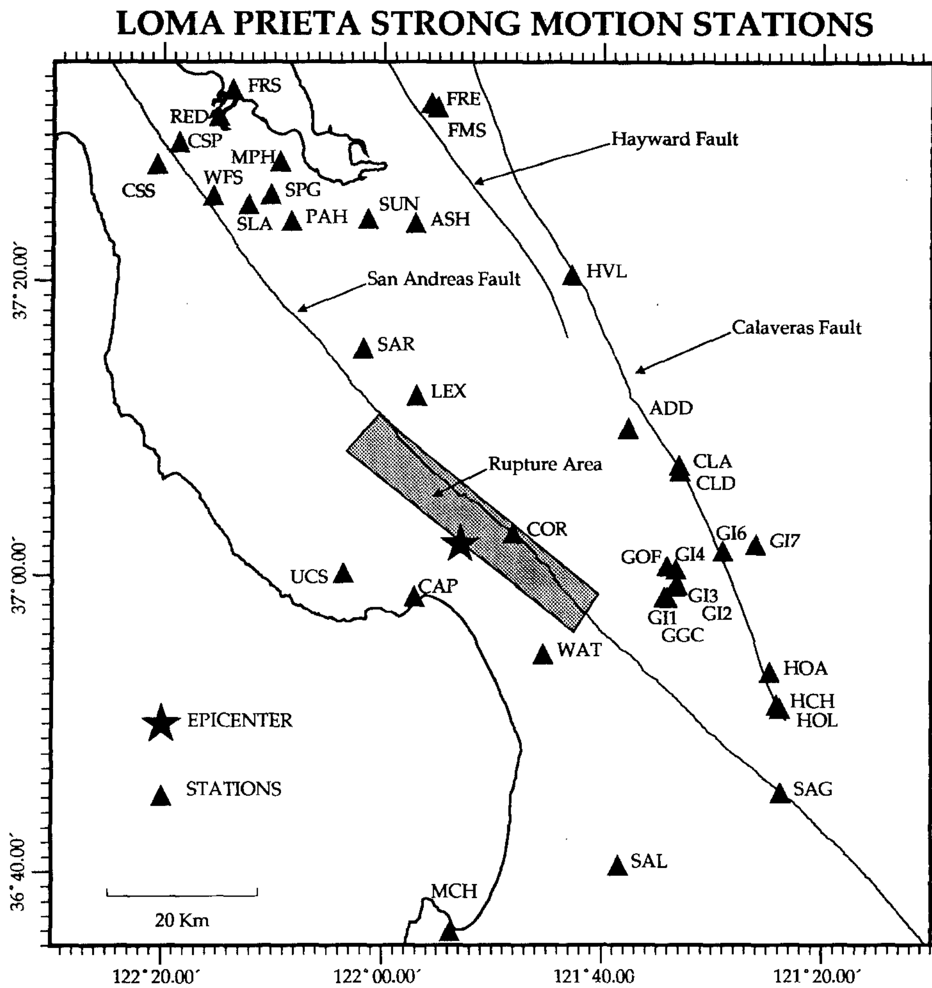

FIG. 1. Map of the region affected by the Loma Prieta earthquake showing the location of strong motion stations used in this study and surface projection of the inferred rupture area. See Table 1 for station names and codes.

et al., 1984). The subfault synthetic time histories were filtered and interpolated in exactly the same manner as the data. For each station subfault synthetics were summed to produce a total synthetic. Each subfault has a time delay that takes into account the rupture time, the time at which slip initiates on the subfault. The station synthetics were aligned with the data by matching the arrival time of the direct *S* wave off the hypocenter subfault with the arrival time of the direct *S* wave in the data. Some errors may have been introduced at this stage for stations with an emergent *S* wave.

Although the slip amplitude is linearly related to the data (e.g., Spudich, 1980), rupture time is nonlinearly related to the observed seismic amplitudes (Archuleta, 1984). Variations in the rupture velocity affect the phase of radiation arriving at a single station. Variation in rupture velocity can be accounted for by either allowing a fault segment to slip repeatedly for a constant rupture velocity or by including the rupture velocity as a parameter in the model.

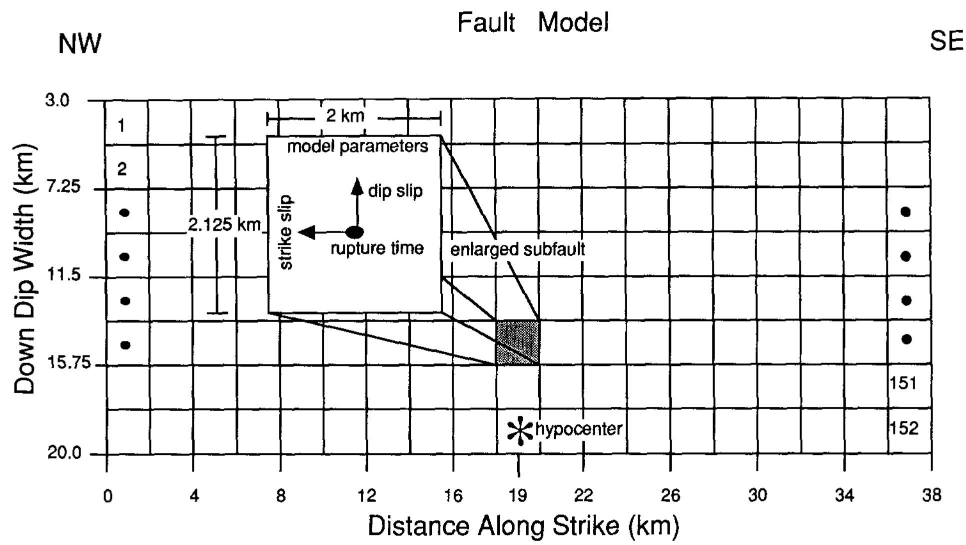

FIG. 2. Parameterization of the fault model used in this study. A total of 152 subfaults with equal dimensions (2 by 2.125 km) are shown in the down-dip perspective. Inversion parameters are shown on the enlarged subfault.

TABLE 2

ONE-DIMENSIONAL VELOCITY STRUCTURE

Depth Interval (km)	V_p (km/sec)	V_s (km/sec)	Density (gm/cm^3)	Thickness (km)
0.0–0.5	3.34	1.67	2.5	0.5
0.5–1.0	4.23	2.2	2.6	0.5
1.0–3.0	5.01	2.89	2.65	2.0
3.0–5.0	5.63	3.25	2.72	2.0
5.0–7.0	5.89	3.4	2.76	2.0
7.0–9.0	6.24	3.6	2.79	2.0
9.0–13.0	6.26	3.61	2.8	4.0
13.0–18.0	6.3	3.64	2.82	5.0
18.0–25.0	6.69	3.86	2.9	7.0
25.0–	8.0	4.62	3.2	

Changes in the rupture velocity produce seismic radiation just as slip itself does (Madariaga, 1977; Bernard and Madariaga, 1984; Spudich and Frazer, 1984). Consequently, changes in the rupture velocity contribute to the observed seismogram and should be included as an unknown in the model.

The waveform inversion technique used in this study is a linearized iterative least-squares inversion that determines both the spatial and temporal dynamic characteristics of the rupture process (Hartzell, 1989). The starting models used in this study have small uniform slip and constant rupture velocity over the entire fault. We considered starting models that have initial rupture velocities of 2.5, 2.8, and 3.0 km/sec. The slip-rate functions used are isosceles triangles with a pulse width of 0.5, 1.0, 1.5, and 3.0 sec. Subfault synthetics for strike-slip (180° rake) and dip-slip (90° rake) mechanisms were generated for all 152 subfaults, for all components at every station. These subfault synthetics are summed to generate the complete station synthetics. Slip amplitude and rupture velocity perturbations were determined simultaneously for each subfault at each iteration by solving an overdetermined system of linear equations. The model was updated and new synthetics calculated using the new perturbed model. This was done iteratively until further iterations failed to provide a significant reduction in the residual error (Euclidean norm between data and synthetics). The strike-slip component was constrained to be right lateral, and the dip-slip component was separately constrained to be reverse slip or thrust. Both have minimization and smoothing constraints as in Hartzell and Iida (1990).

Results

The solutions presented in this article are the result of a systematic inversion scheme to search the model parameter space as completely as possible for a global minimum in the residual error. Differences in the initial rupture velocity are examined in the first set of inversions along with variations in the width of the slip rate function (rise time). The station coverage is then changed along with the length of the inversion time window. Finally the number of components is changed to include all three components of the particle velocity time histories. A summary of the results for all inversions is given in Table 3. One important result is that there are general characteristics of all the models which are found to be consistent throughout the set of inversions.

Slip Distribution

Contours of the slip distribution and the rupture times, projected on the fault plane, are shown in Figure 3. These contours represent the best fitting solution

TABLE 3

Nonlinear Inversion Results

Model	Initial Rupture Velocity (km/sec)	Rise time (sec)	$\bar{U}$ Dip-slip (cm)	$\bar{U}$ Strike-slip (cm)	$\bar{U}$ Total slip (cm)	Moment ($\times 10^{26}$ dyne-cm)	Residual Error
1	2.5	0.5	61	65	105	2.55	28.542
2	2.5	1.5	65	62	103	2.47	28.689
3	2.8	0.5	52	58	91	2.21	28.418
4	2.8	1.5	62	62	103	2.47	28.409
5	3.0	0.5	57	58	96	2.33	28.601
6	3.0	1.5	64	66	110	2.62	28.312
7*	3.0	0.5	46	53	83	2.03	20.456
8*	3.0	1.5	58	58	97	2.35	20.080
9*†	3.0	1.5	61	58	101	2.42	18.080
10†§	2.5	0.5	76	70	121	2.89	17.956
11†	3.0	3.0	73	66	114	2.68	18.230
12‡	2.8	0.5	52	51	85	2.07	23.423
13†	3.0	1.0	57	57	97	2.34	18.247
14‡	3.0	1.0	52	57	92	2.23	23.090
15†	3.0	1.0	62	51	94	2.25	18.795

* 20 stations, 35-sec inversion window.

† 20 stations, 20-sec inversion window.

‡ 20 stations, 20-sec inversion window, horizontal and vertical components (60 records).

§ 40 iterations.

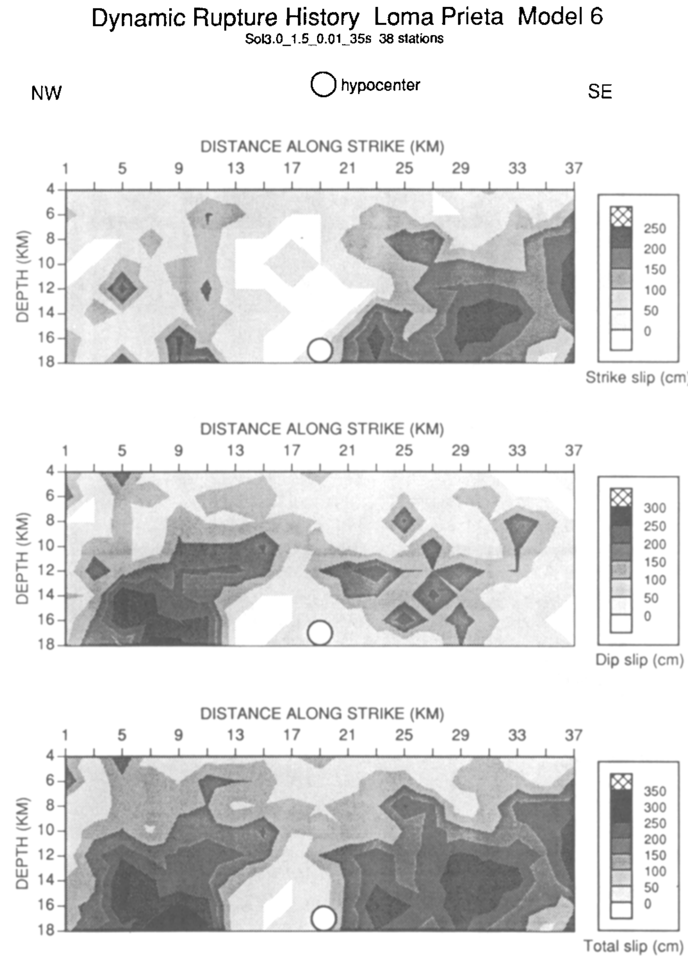

(a)

FIG. 3. (a) Model 6: fault slip determined by inverting 76 horizontal time histories (35.0 sec) of ground velocity. Cross section of the fault plane with depth shown looking perpendicular to the fault from the southwest, i.e., variables are plotted on the footwall. Strike slip, dip slip, and total slip (cm) are shown as shaded contours on the fault plane. This is our preferred model of the slip parameters describing the rupture history of the Loma Prieta earthquake. (b) Model 6: rupture front determined by inverting 76 horizontal time histories (35.0 sec) of ground velocity. The position of the rupture front is contoured in 1.0-sec intervals on the footwall. Upper figure is the initial starting model in the nonlinear inversion showing the rupture front for a constant rupture velocity of 3.0 km/sec. The lower figure is the position of the rupture front determined by the inversion of the data. The lower figure is our preferred model for the evolution of the rupture.

for all 38 stations, using horizontal components only (model 6, Table 3). This model has initial rupture times based on a constant rupture velocity of 3.0 km/sec. The rise time for each slip function is a constant, 1.5 sec. Models that have initial rupture velocities of 2.5 and 2.8 km/sec have larger perturbations to the rupture front, always speeding up the rupture propagation. Thus, an initial rupture velocity of 3.0 km/sec provides a solution with the least perturbation to the rupture times. Solutions for different initial conditions (models 1 to 5, Table 3) have the same general slip distribution with slightly larger residual errors. One general characteristic of model 6 is the bimodal

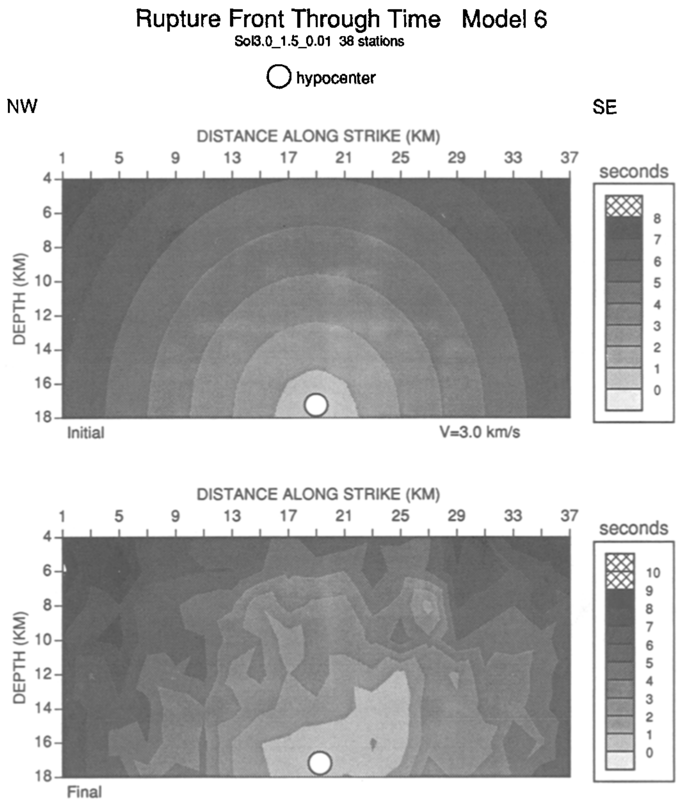

(b)

FIG. 3. (*Continued*).

distribution of slip (Fig. 3a). The patch to the north of the hypocenter is predominantly dip slip; the patch south of the hypocenter is predominantly strike slip. Another general feature in this model is the lack of any significant slip just to the north and up dip from the hypocenter.

When the station coverage is reduced from 38 to 20 stations (Fig. 4, Table 1), the same general characteristics of the slip distribution remain (Fig. 5a). This suggests that the solution is relatively stable with regard to this set of stations. This may be due to the fact that most of the stations are outside the immediate epicentral region; only six stations are near the surface projection of the fault plane (Fig. 1). The stations eliminated from the later inversions were chosen by comparing the synthetics with the data. Stations that were not on hard rock sites were fit poorly because no correction is made for site response. These were removed first. In order to keep a few of the stations at large epicentral distances, some of the more proximal stations were removed. Independent studies using strong motion data (Beroza, 1991; Wald *et al.*, 1991) with different station distributions and different methods, as well as studies using only teleseismic data (Hartzell *et al.*, 1991), have produced similar results. Although the distributions of strike-slip and dip-slip motions are slightly different, the bimodal nature of the slip distribution can be seen in each of these studies.

A concern with the solutions presented in Figures 3a and 5a is the effect

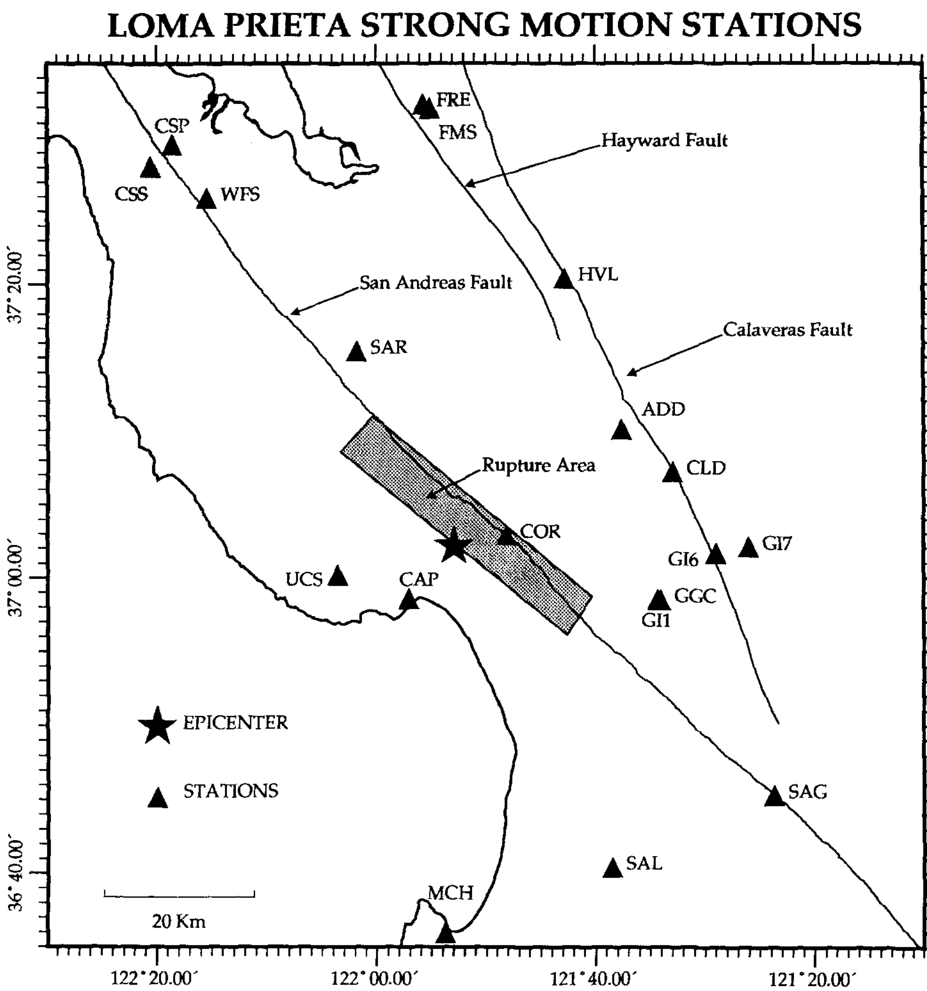

FIG. 4. Station distribution for inversions which use only 20 of the 38 stations shown in Figure 1. Models 7 to 15 (Table 3) use this station distribution. Surface projection of the inferred rupture area shown as shaded rectangle. See Table 1 for station names and codes.

produced by the latter part of the time histories. The farther along in time on the data record, the greater the likelihood that path and site effects dominate the record compared to source characteristics. To examine this question, we inverted only the first 20.0 sec of the time histories rather than 35.0 sec. The results of this inversion (model 9) are shown in Figure 6a. These results can be directly compared to those shown in Figure 5a. The solutions are almost identical with the slight differences being less than the resolution of the inversion technique (discussed later). The general characteristics of the distribution of slip remained unchanged.

At this point the differences in the rise time were examined. Synthetic time histories computed for 0.5-, 1.5-, and 3.0-sec rise times (models 7, 9, and 11, Table 3) are compared with the data for four stations (Fig. 7a and 7b). With a maximum frequency of 1.0 Hz in both the data and the synthetics, the 0.5-sec rise time is seen as almost a delta function and always fits the high-frequency content well. Solutions based on a 3.0-sec rise time produced synthetics that

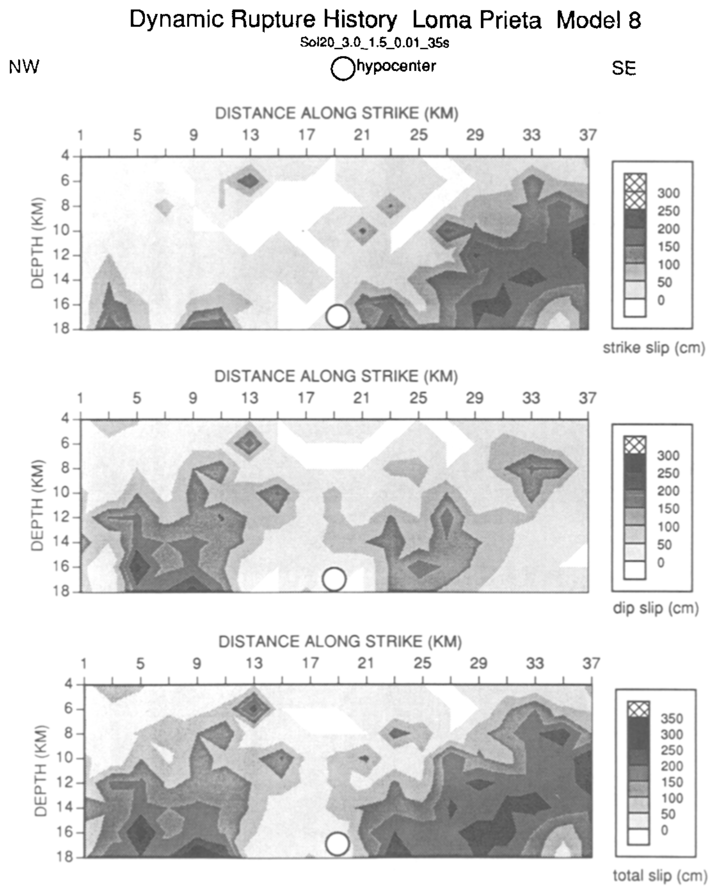

(a)

FIG. 5. (a) Model 8: fault slip determined by inverting 40 horizontal time histories (35.0 sec) of ground velocity. Strike slip, dip slip, and total slip (cm) are contoured on the footwall. Compare this with Figure 3a for which 76 horizontal time histories were inverted. (b) Model 8: rupture front determined by inverting 40 horizontal time histories (35.0 sec) of ground velocity. Compare this with Figure 3b for which 76 horizontal time histories were inverted.

reproduced the low-frequency content but did not match the details of the waveforms. The 1.5-sec rise time is the best of the three trial rise times, but it still seems to lack some of the details found in the synthetics based on the 0.5-sec rise time. Because the data seem to fall between the synthetics from 0.5- and 1.5-sec rise times, a 1.0-sec rise time was then examined and found to produce the least residual error. All subsequent inversions were based on a 1.0-sec rise time.

With the number of stations reduced to 20, the inclusion of the vertical components became computationally efficient (the numerical problem could be contained inside RAM). The effect this had on the solution is seen by comparing Figures 6a and 8a (models 9 and 14, Table 3). The absolute slip magnitudes for model 14 (Fig 8a) are scaled by a factor (amplitude scale factor) of 1.5, relative to those of Figure 6a. Because of the minimization involved, the slip magnitudes are underestimated by the inversion technique. The amount of scaling is subjective (see discussion) and has only been used in Figure 8, the final

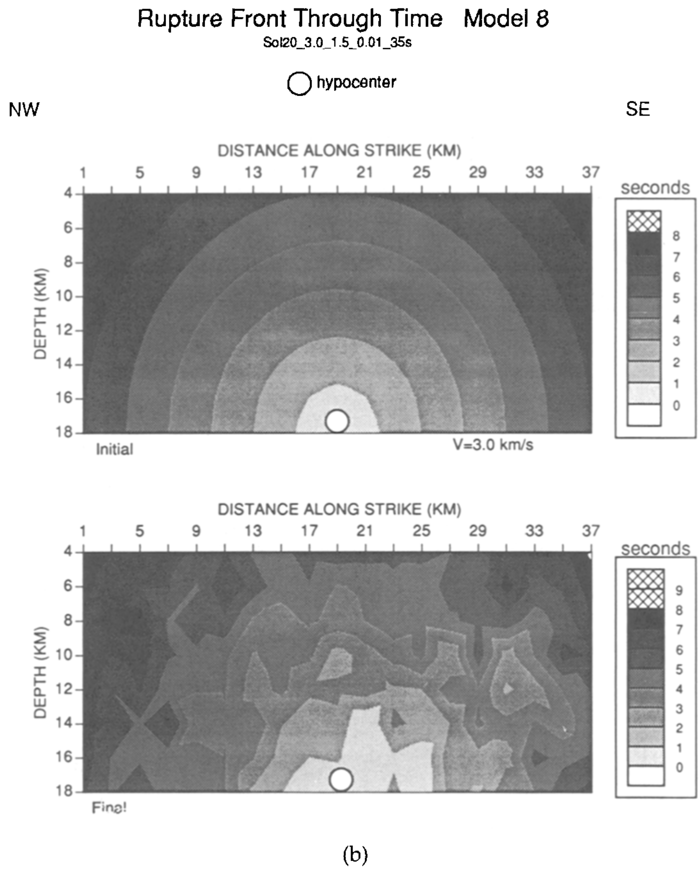

FIG. 5. (*Continued*).

solution. The magnitude and overall slip distribution of Figures 6a and 8a are similar; the general characteristics of the solution are preserved. The one significant difference is that the use of vertical components puts a greater amount of slip at depths of 7 to 10 km on the northern half of the rupture area (Fig. 8a).

The rake vector for the southern and northern halves of the fault clearly show a rotation in all of the models. When the southern half of the fault is taken alone, the rake is 156° (180° = pure right lateral slip). This is larger than the value of 135 ± 10° found in teleseismic and longer period studies (Choy and Boatwright, 1990; Kanamori and Satake, 1990; Romanowicz and Lyon-Caen, 1990; Zhang and Lay, 1990; Wallace *et al.*, 1991). When the northern half of the fault is taken alone, the rake is 115° (90° = pure thrust), smaller than the far-field results. When the whole fault is taken as one, the rake angle is 137°, a nearly equal partitioning of strike-slip and dip-slip motion. The far-field data seem to show an average of the rake for the bimodal slip distribution.

Rupture Propagation

The variations in rupture velocity are shown for each of the above mentioned models (Fig. 3b, 5b, 6b, and 8b). The propagation of the rupture front through

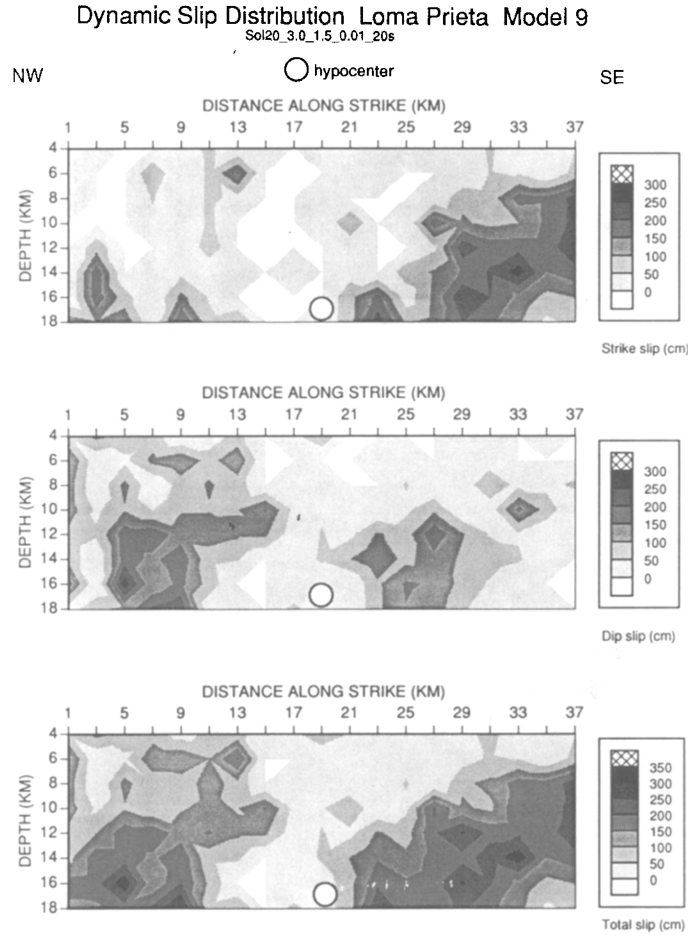

(a)

FIG. 6. (a) Model 9: fault slip determined by inverting 40 horizontal time histories (20.0 sec) of ground velocity. Strike slip, dip slip, and total slip (cm) are contoured on the footwall. Compare this with Figure 5a for which 35.0 sec of record were inverted. (b) Model 9: rupture front determined by inverting 40 horizontal time histories (20.0 sec) of ground velocity. Compare this with Figure 5b for which 35.0 sec of record were inverted.

time is clearly bilateral. A common characteristic of all the solution models is an apparent increased rupture velocity to the south and up dip from the hypocenter. Initial rupture velocities of greater than 3.4 km/sec are seen as the rupture front propagates from the hypocenter to the south. The average rupture velocity over the entire fault is closer to 3.0 km/sec. A consistent result for all inversions is that the main release of energy is within the first 7.0 sec of dynamic slip. The more complex aspects (roughness) of the rupture propagation (Fig. 3b, 5b, 6b, and 8b) may not be resolvable by the inversion method. One critical aspect of the rupture velocity is that the slip to the northwest, predominantly thrust, is radiating energy between 3.0 to 7.0 sec, almost simultaneously with the slip to the southeast, predominantly strike slip, also radiating energy between 3.0 and 7.0 sec. This may present unusual complications in the teleseismic signal when it comes to resolving the differences in rake between

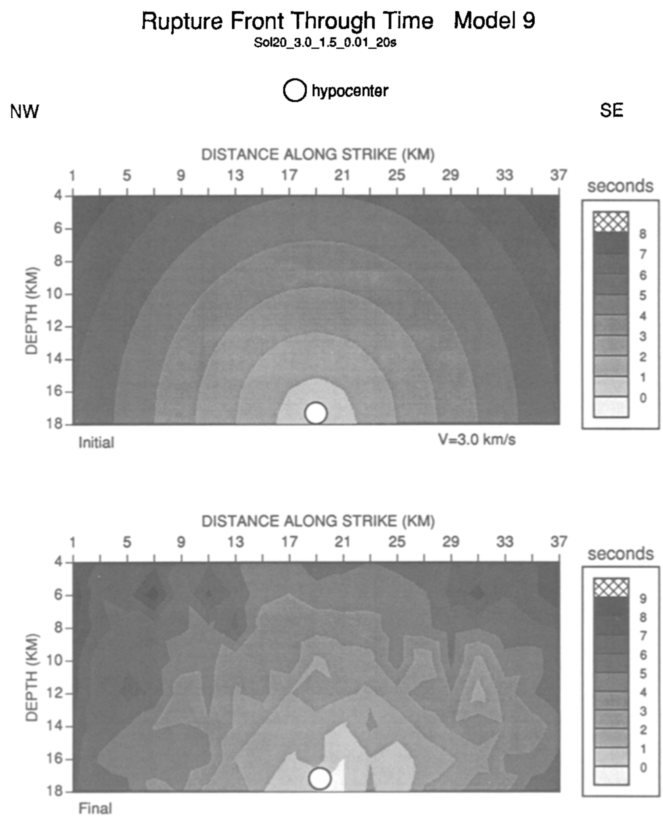

(b)

FIG. 6. (*Continued*).

the two patches. Solutions of the source mechanism from far-field data would tend to average the two patches.

Synthetics

The fit between the data and the synthetic time histories is shown in Figures 9a to e. The data and synthetics represent the 20 stations from model 14. In general, the first 15.0 to 20.0 sec of data are matched both in amplitude and shape for stations without strong site effects. The contribution to the model from the last 15.0 sec of data was determined to be insignificant by running inversions with a 20.0-sec inversion window. Some of the stations that were eliminated for the second set of inversions show large site effects and are not fit well by the synthetics. All of the Hollister stations have these site effects and are probably related to the thick (> 3000 m) sequence of Pliocene sediments on which the stations are located. The fit in amplitude to other stations supports strong site effects in the Hollister records and suggests that the large amplitudes are not coming from the source. Some stations in the San Francisco Bay area also show site effects and are not fit well by the synthetics. Future work may include modeling of specific site structures in an attempt to distinguish between, and to extract, source characteristics from records heavily overprinted by site effects.

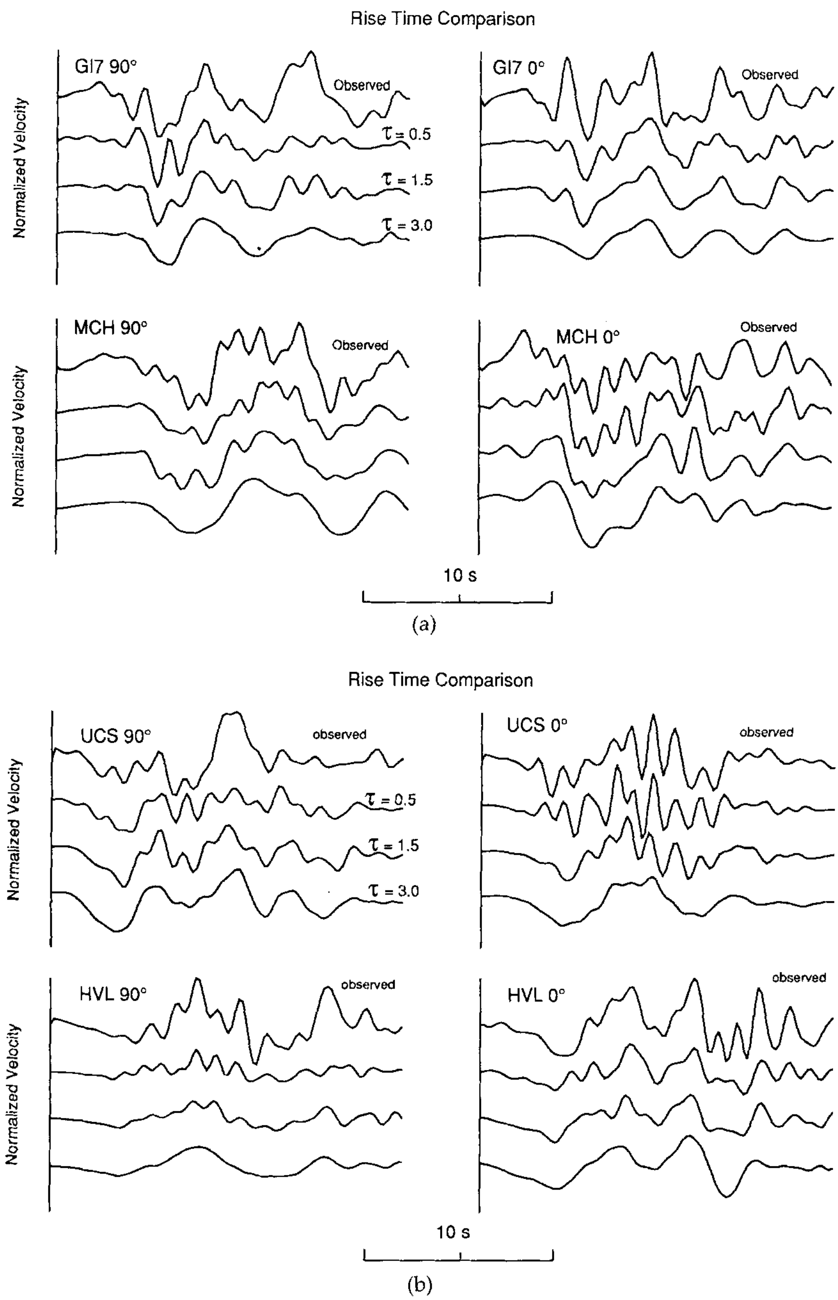

FIG. 7. (a) Particle velocity time histories resulting from assumed rise times of 0.5, 1.5, and 3.0 sec (models 7, 9, and 11, Table 3) are compared with records at stations Gilroy #7 and Monterey City Hall (Fig. 1, Table 1). To compare the phase between synthetic and data each record has been normalized by its peak value and plotted to the same scale. Top trace is the observed data. The next three traces are synthetics with rise times of 0.5, 1.5, and 3.0 sec. These comparisons suggest a rise time between 0.5 and 1.5 sec. (b) Same as Figure 7a except that stations UC Santa Cruz and Halls Valley (Fig. 1, Table 1) are shown.

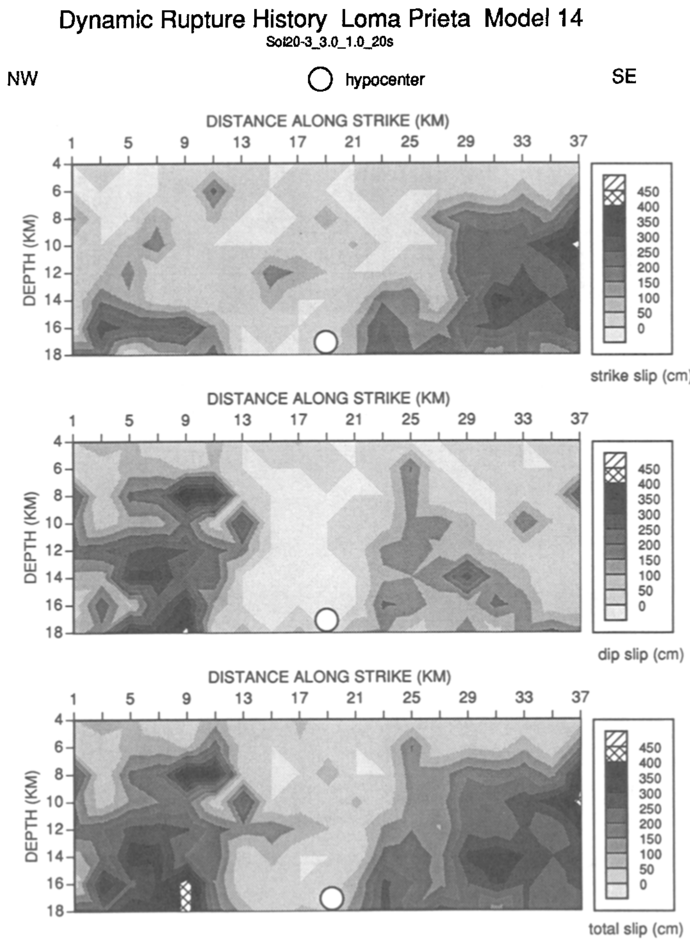

(a)

FIG. 8. (a) Model 14: fault slip determined by inverting 40 horizontal time histories and 20 vertical time histories (20.0 sec) of ground velocity. Strike slip, dip slip, and total slip (cm) are contoured on the footwall. Compare this with Figure 6a for which only the horizontal components were inverted. (b) Model 14: rupture front determined by inverting 40 horizontal time histories and 20 vertical time histories (20.0 sec) of ground velocity. Compare this with Figure 6b for which only the horizontal components were inverted.

Error Analysis and Resolution of the Method

Error estimates of the model parameters and resolution of the inversion method are addressed in Figures 10 to 12. These estimates are calculated as in Hartzell and Iida (1990). The error estimates are for a given tolerable misfit to the data. They represent bounds on the model parameters that would result from a perturbation of the data by 10% of the Euclidean norm of the fit to the data. The large patches of zero uncertainty are where the model values are zero. Estimates in the uncertainty of strike-slip motion, dip-slip motion, and rupture times for model 14 are shown in Figure 10. The uncertainty in slip amplitude is about 40 cm and the uncertainty in rupture time is about 0.8 sec. This suggests that details in the solution on the order of these estimates should not be considered as significant. Thus, for Figures 3, 5, 6, 8, and 13, slip contours are

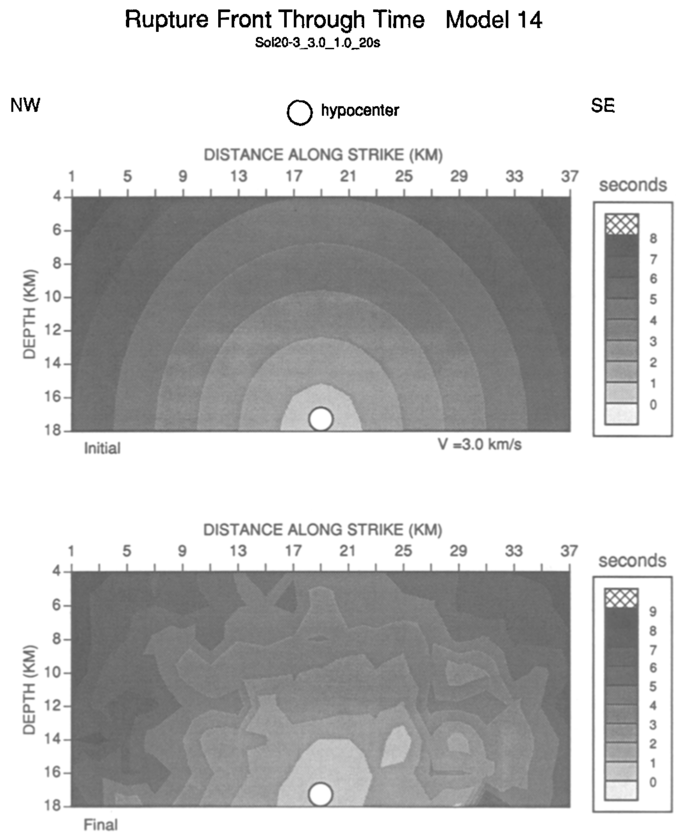

(b)

FIG. 8. (*Continued*).

shown at 50-cm intervals and rupture time contours are shown at 1.0-sec intervals.

The resolution of the inversion technique is estimated by running test inversions with synthetic data. In these cases, we used the station distribution of Figure 4 and inverted all three components. We first examined the situation where the slip, both strike slip and dip slip, is maximum at the hypocenter and monotonically decreases away from the hypocenter (*top* part of Fig. 11a). This slip model is used to generate synthetic data that is later inverted. The results of the inversion for the strike-slip and dip-slip distribution are shown in the *middle* and *bottom* parts of Figure 11a. The rupture times based on a constant rupture velocity (3.0 km/sec) used to generate the synthetic data are shown in the *top* portion of Figure 11b. The initial starting model assumed a constant rupture velocity (2.5 km/sec), shown in the *middle* part of Figure 11b. The result of the inversion is shown in the *bottom* part of Figure 11b. The slip distribution used as a starting model in the inversion is the same as that used with real data, a number near zero for the entire fault. This example shows that there are tradeoffs between slip amplitudes and rupture velocity. The inversion predicted slip amplitudes 35% higher than the actual model. The distribution of slip was confined to a smaller area, rather than increasing the rupture velocity

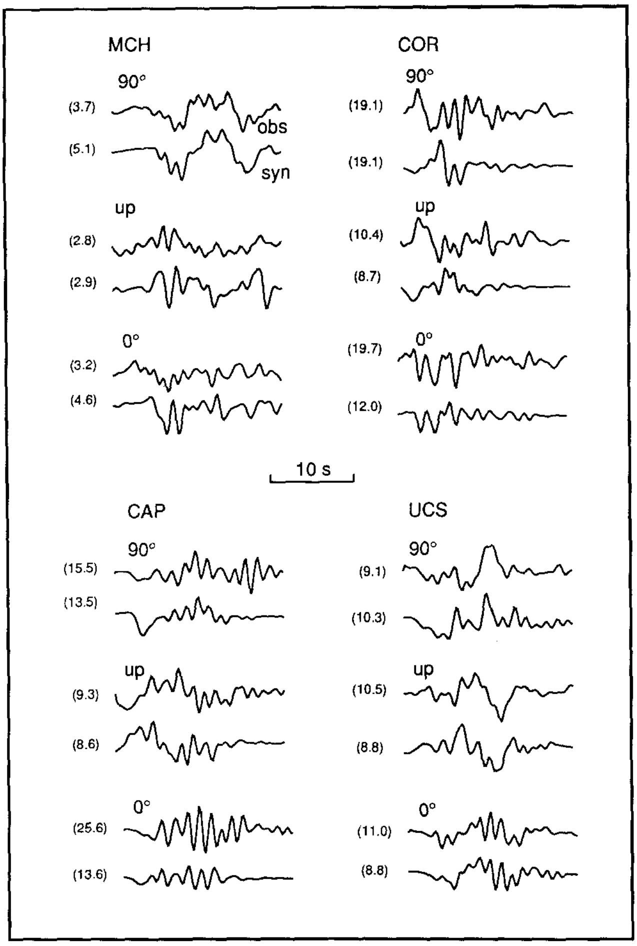

FIG. 9. (a) The three components of particle velocity at stations MCH, COR, CAP, and UCS (Fig. 1, Table 1) are compared with synthetics generated by model 14 (Fig. 7a and b, Table 3). For each component, the upper trace is the data and the lower trace is the synthetic. Each component is labeled with the direction of positive motion measured clockwise from North. The peak amplitude (cm/sec) is given in parenthesis to the left of each time history. The three components of particle velocity at stations (b) GI6, GI7, SAL, and SAG; (c) FMS, HVL, WFS, and CSP; (d) CSS, FRE, SAR, and CLD; and (e) ADD, ADL, GGC, and GI1 (Fig. 1, Table 1) are compared with synthetics generated by model 14 (Fig. 7a and b, Table 3). (See Fig. 9a for details.)

and moving the slip out to the sides. The solution appears to be nonunique in this case.

A bimodal source is used as a test inversion to determine the resolution for the Loma Prieta event. The top portion of Figure 12a shows the slip distribution used to generate synthetic data for this case. The hypocenter contains a small amount of slip that increases outward into two large patches with a gap up dip from the hypocenter. The bottom portion of Figure 12a shows the solution determined by the inversion technique. In this case, slip occurs on larger patches but its amplitude is underestimated by 20%. The rupture velocity used to generate the synthetic data (3.0 km/sec) is shown on the *top* portion of Figure 12b and is the same as the previous test case. As before, the rupture velocity used as a starting point for the inversion is a constant 2.5 km/sec

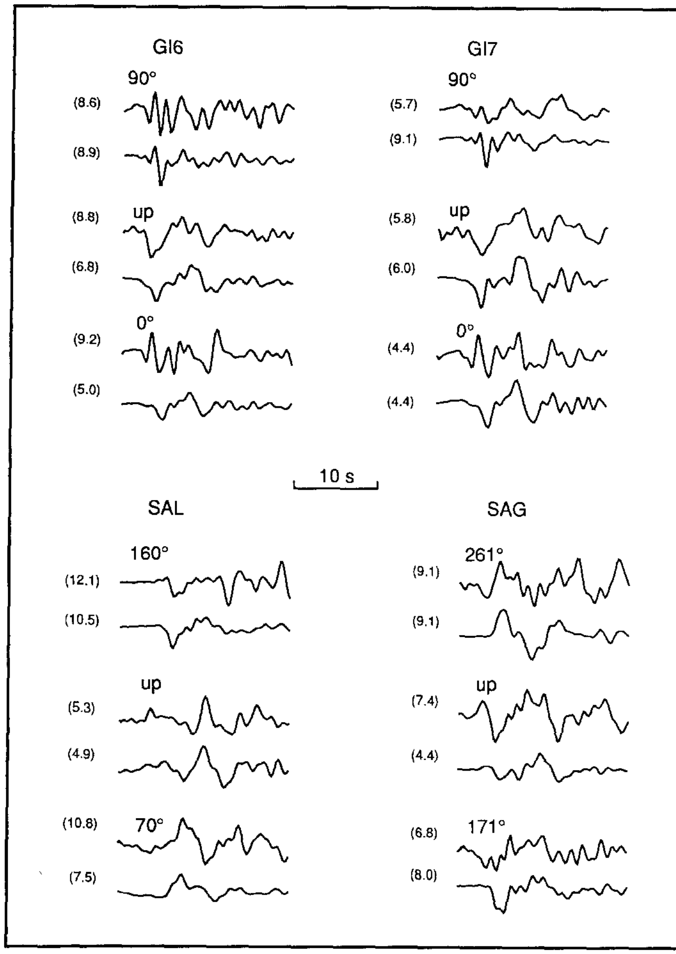

(b)

FIG. 9. (*Continued*).

(*middle* part, Fig. 12b). The *bottom* part of Figure 12b shows the final rupture time determined by the inversion. In this particular case, rupture time perturbations are greater and in the direction of the actual model. The region of zero slip between the two patches produces roughness in the rupture front solution because the inversion has no information where there is no slip. The ability to resolve the general features of the synthetic models presented in this section supports the resolution of the general characteristics found in the Loma Prieta data, namely, that the uncertainty in slip is about 40 cm and the uncertainty in rupture time is about 0.8 sec.

Timing

The timing of the strong motion data in this study is relative, although absolute times are available for some of the stations. The presence of a foreshock 2 sec before this event has been demonstrated by Wald *et al.* (1991) and has affected the timing of at least some of the stations. The hypocentral location used in this study is that of the USGS, which is from the local high-gain

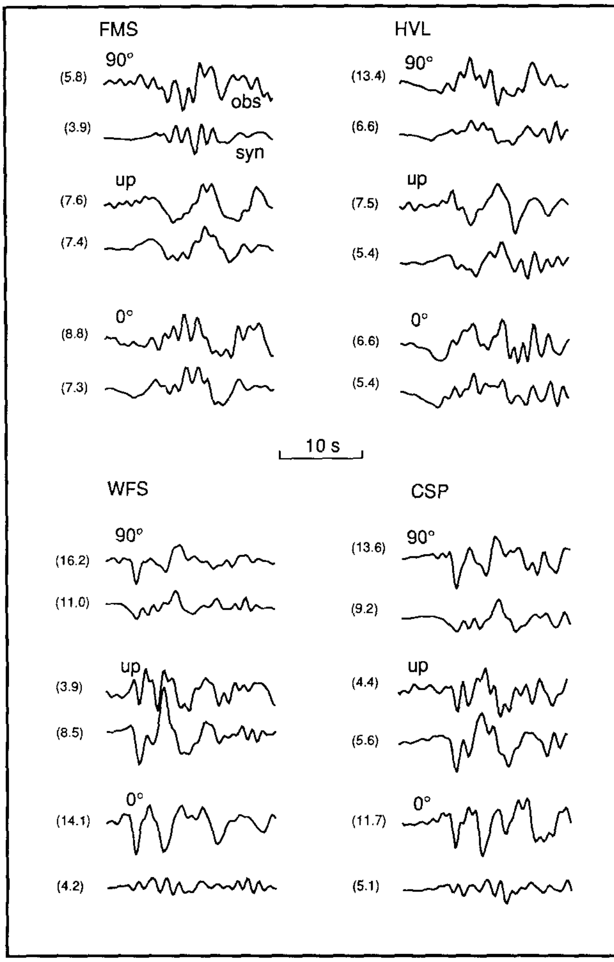

(c)

FIG. 9. (*Continued*).

network that triggered on the foreshock. Since these instruments saturated on the foreshock, the location and the timing of the mainshock were masked by the foreshock. It seems likely that this early foreshock evolved into the Loma Prieta earthquake. Since we are aligning the S wave from the "hypocenter" subfault with the S wave in the data, this energy may not actually be coming from the "hypocenter" subfault but from a region shifted slightly on the fault plane. Thus, there is some question as to the location of the mainshock hypocenter and the timing of the data records. There could be as much as a few seconds error in the alignment of the synthetics with the data.

Wald *et al.* (1991) use absolute timing and account for this 2-sec timing difference due to the foreshock. The slip distribution from an inversion using this timing scheme is shown in Figure 13. For stations without absolute time, a correction to the timing was applied based on the timing of the stations with absolute time. Figure 13 demonstrates the stability of the slip distribution with respect to a time shift in the synthetics. The strike-slip motion on the southern half of the fault has moved away from the fault edge, but otherwise the solution

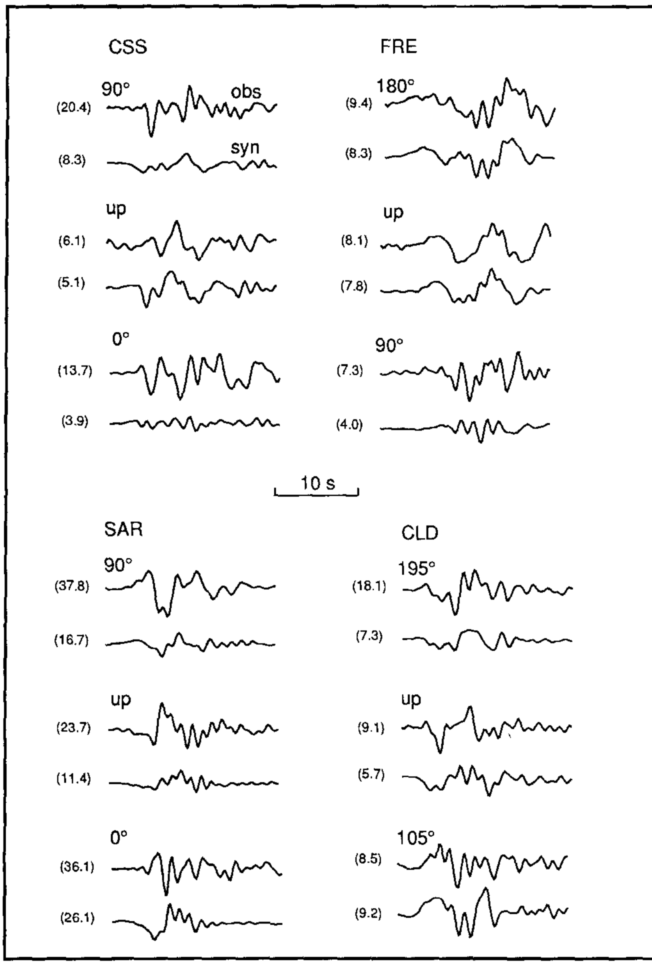

(d)

FIG. 9. (*Continued*).

looks very similar to the other models presented in this study. The rupture velocity (not shown) also remained very similar.

DISCUSSION

The static slip distribution is interesting when compared with the distribution of aftershocks and the distribution of aftershock mechanisms. Aftershocks viewed in cross section perpendicular to the San Andreas fault align on a steeply dipping plane at the northern end of the fault zone. This alignment becomes shallower and steeper, and it approaches vertical to the south beyond the southeastern edge of the inferred rupture area (Dietz and Ellsworth, 1990). The aftershock mechanisms change as a function of position along the fault as well. Aftershocks along the northern end exhibit predominantly reverse mechanisms on planes nearly parallel to the San Andreas, while aftershocks on the southern end exhibit predominantly right-lateral mechanisms. The great diversity of aftershock mechanisms is in support of a very nonuniform slip distribution (Oppenheimer, 1990). The change in rake moving from the southern end of

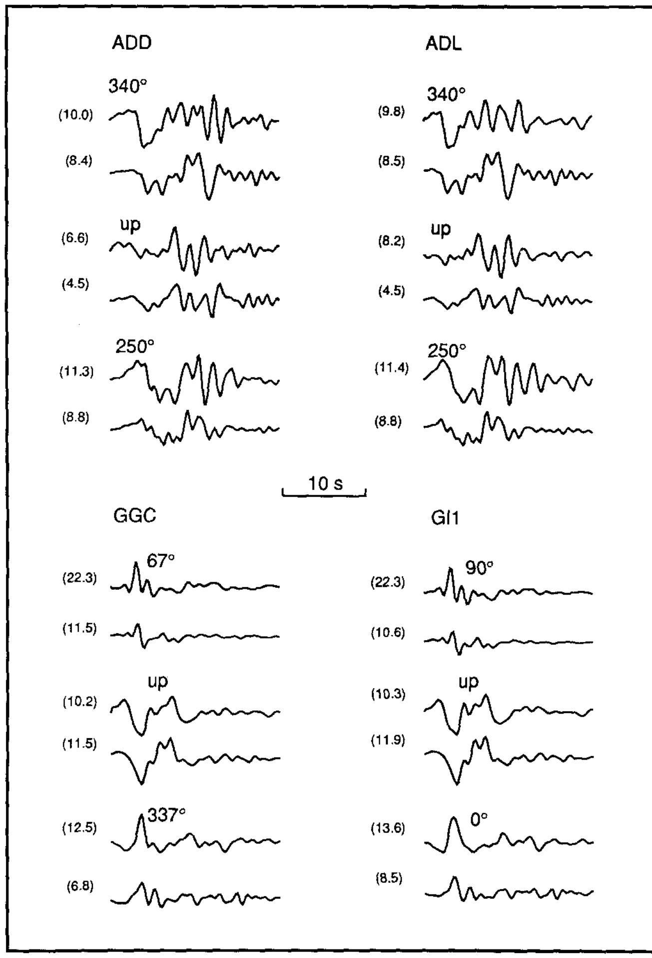

(e)

FIG. 9. (*Continued*).

the rupture area to the northern end is consistent with these aftershock mechanisms. The aftershocks outline a fault plane that has a finite width of 2.0 km. The faulting may be occurring over a finite width rather than on a single planar fault. Geometrical problems are created by this change in rake, which may be an explanation for this aftershock distribution and variation in mechanisms.

Another interesting result is that the inversion does not require slip at shallow depths to fit the synthetics. This corresponds well with the idea that the rupture did not break the free surface and probably did not propagate to depths shallower than 5 km. The magnitude of total slip (Table 3) is less than that required by the geodetic data. The geodetic data require 1.6-m right-lateral strike slip and 1.2-m reverse slip (Lisowski *et al.*, 1990). The average total slip determined in this study is 1.35 to 1.65 m. The reverse slip and right-lateral strike slip is partitioned nearly equal for all models and ranges from 0.75 to 0.95 m. These values are an average of all models in Table 3, adjusted by the amplitude scale factor mentioned in the previous section. Although the fault

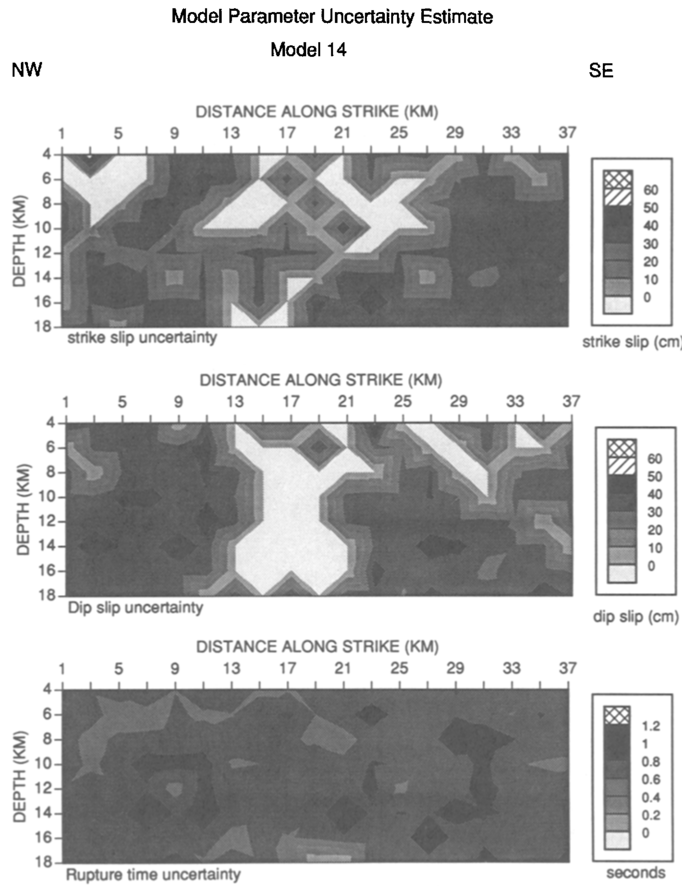

FIG. 10. Uncertainty estimate for model parameters determined from model 14. Strike-slip, dip-slip, and rupture time uncertainty are shown as shaded contours on the footwall.

area used in the geodetic model is 20% smaller than the area used in this study, this does not account for all of the slip deficiency. Geodetic modeling of the static displacement produced a best-fitting model with uniform strike-slip and dip-slip distributions on a fault parallel to, but offset from, the seismicity. The use of a uniform elastic half-space with uniform slip on the fault in the geodetic studies may be overestimating the average slip magnitudes. One result consistently found for all models is that the slip magnitude is not 2.0 m at shallow depths (5 to 10 km), as in the geodetic studies (Lisowski *et al.*, 1990). Also, the time interval sampled in this study is constrained to dynamic rupture (about 8.0 sec), while the geodetic data is sampling a much larger time interval, 2 weeks being the shortest time between reoccupation of benchmarks.

The minimization, which is inherent to the inversion technique, provides us with minimum bounds for the estimation of slip and moment. The combination of reducing the fault area and scaling to account for the inversion minimization would give slip values closer to the geodetic results. A minimum estimate of moment is $2.3 \pm 0.3 \times 10^{26}$ dyne-cm (Table 3) with all of the moment release in the first 7.0 sec of the event. The moment estimate obtained after including the amplitude scale factor is $3.5 \pm 0.5 \times 10^{26}$ dyne-cm. The amplitude scale factor

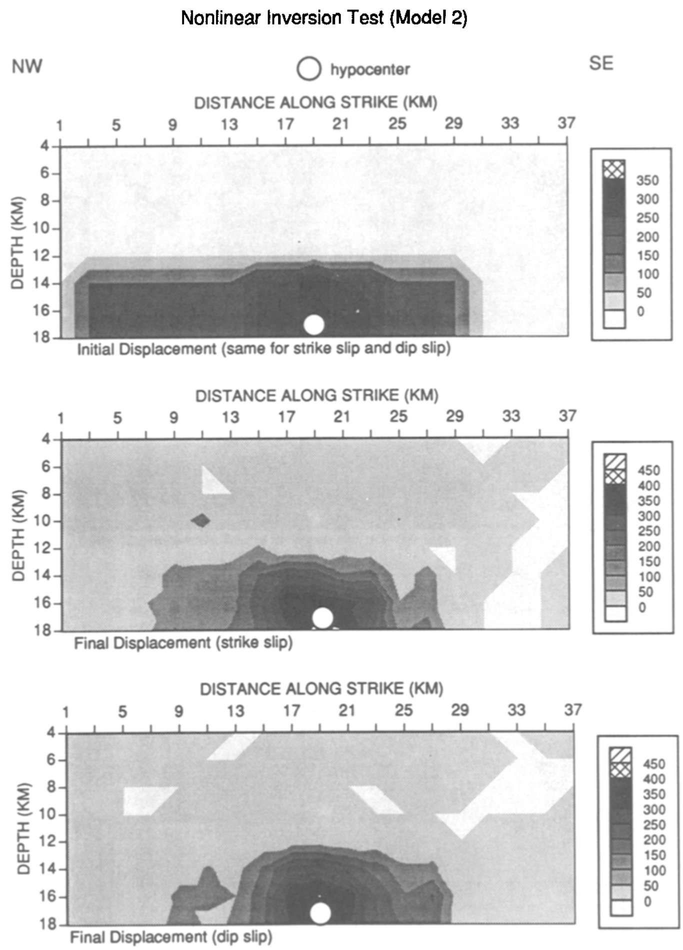

(a)

FIG. 11. (a) Nonlinear inversion test (model 2). An assumed slip distribution (*top figure*, initial displacement, cm), both strike slip and dip slip having the same distribution on the fault, was used to calculate synthetics. The synthetics from the assumed model were inverted to find a model consistent with these time histories. The inversion resulted in strike-slip (*middle figure*) and dip-slip (*bottom figure*) values (cm) that are contoured on the footwall. See text for discussion. (b) Nonlinear inversion test (model 2). Along with the assumed slip distribution (Fig. 11a), the test model has a prescribed rupture evolution (*top figure*). The starting model for the inversion is shown in the *middle figure*. The result of the inversion is shown in the *bottom figure*. All contours, in seconds, are plotted on the footwall. See text for discussion.

of 1.5 calculated for model 14 is simply the ratio of root-mean-square (rms) amplitudes between the data and the synthetics for stations that contain the least site effects. There is some subjectivity involved with this estimate, which could be removed by including in the Green's functions the site response for each station. This involves calculating separate Green's functions for every station, assuming the site effects are known or using empirical Green's functions.

The differences between this study and other seismological models of the slip distribution (e.g., Beroza, 1991; Hartzell *et al.*, 1991; Wald *et al.*, 1991) stems from the use of different data sets, different station distributions, different timing, and different velocity structure. The grouping of stations at a particular

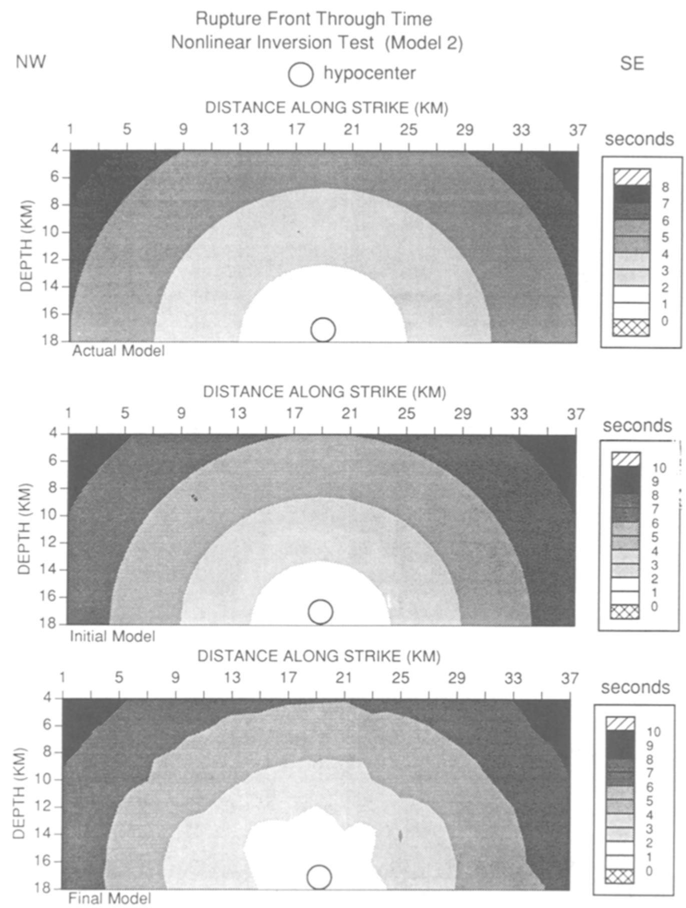

(b)

FIG. 11. (*Continued*).

azimuth will add a bias towards fitting the data at the azimuth. The inclusion of the Santa Cruz portable stations, of which two of the four were north of the hypocenter and on top of the rupture area, adds information to the northern end of the rupture area that is not included in this study. The next stage of the strong motion analysis in this earthquake should look into the effect of different station distributions and take into account site response. The timing and location of the mainshock may be resolved by locating the mainshock with broadband instruments that did not clip during the first 2 sec. It is clear that timing differences can shift the location of the patches of rupture. A more detailed study is needed to determine the errors associated with alignment of the synthetics to the data. The use of a velocity structure with slower velocities in the top kilometer will rotate more energy into the horizontal components, which are under predicted in amplitude at some stations (Figs. 9a to e). This would be better accounted for as site response for stations that are underlain by a slower upper layer, since some of the stations are on hard rock sites for which the present velocity structure is adequate.

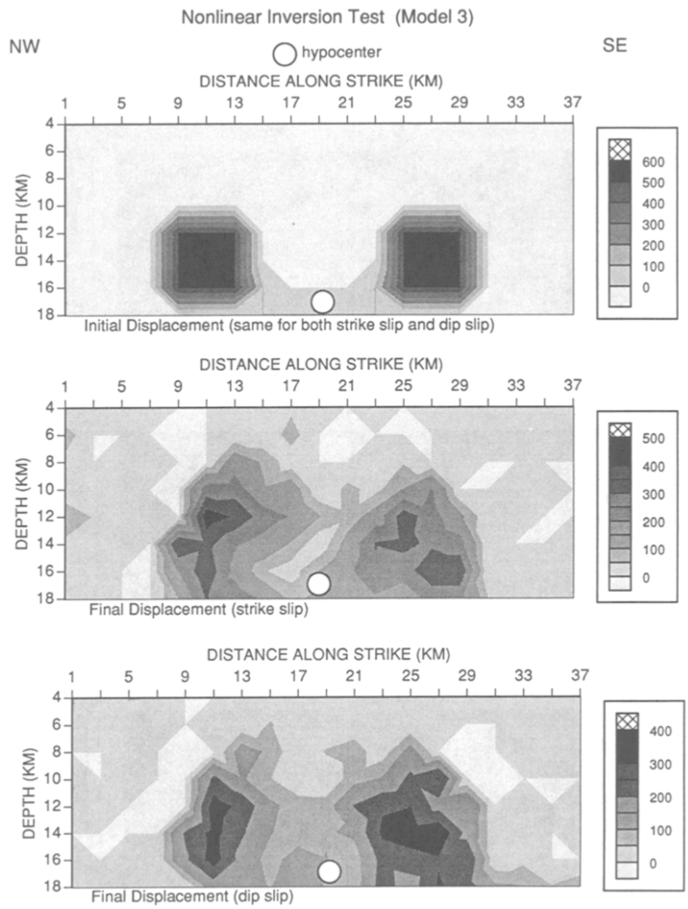

(a)

FIG. 12. (a) A second nonlinear inversion test (model 3). An assumed slip distribution (*top figure*, initial displacement, cm), both strike slip and dip slip having the same distribution on the fault, was used to calculate synthetics. The synthetics were inverted to find a model consistent with these time histories. The inversion resulted in strike-slip (*middle figure*) and dip-slip (*bottom figure*) values (cm) that are contoured on the footwall as compared to the top figure. See text for discussion. (b) A second nonlinear inversion test (model 3). Along with the assumed slip distribution (Fig. 12a), the test model had a prescribed rupture evolution (*top figure*). The starting model for the inversion is shown in the *middle figure*. The result of the inversion is shown in *bottom figure*. All contours, in seconds, are plotted on the footwall. See text for discussion.

Although the distribution of static slip illustrates some of the heterogeneity of the stress release, the earthquake rupture is the process of going from one static stress state to another. The two parameters that are critically important in the earthquake dynamics are the rupture time and the rise time for each point on the fault. We found by trial and error that a rise time of 1.0 sec produced the best fit between the synthetic time histories and the data. This rise time is less than what might be assumed for an earthquake with this size fault plane. Following Day (1982), we estimate a rise time of about 2.0 sec (fault plane width divided by twice the rupture velocity). Yet is was quite clear from the comparisons (Fig. 7a and b) that the rise time is less than 2.0 sec. For the

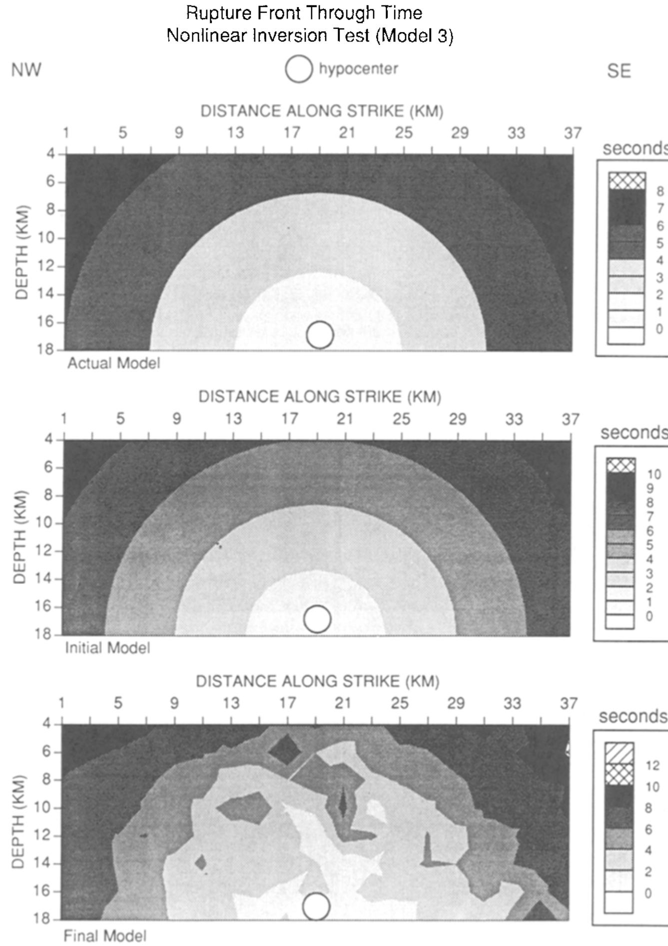

(b)

FIG. 12. (*Continued*).

parameterization used in this study, the slip rate is approximately the static slip divided by the rise time. Because the slip rate is directly proportional to the local stress drop (Brune, 1970), a constant rise time everywhere on the fault implies that the distribution of static slip is also the distribution of local stress release. Because the rise time is not a free parameter in our inversion, we cannot be certain that the rise time is approximately constant over the entire fault plane. For the faulting models we considered, a rise time of 1.0 sec produces the best agreement between the synthetics and the data.

Although the rise time has direct implications with regard to the local stress drop, the rupture time can be more critical in determining the amplitude of the seismic radiation (Anderson and Richards, 1975; Archuleta, 1984). Rupture time is nonlinearly related to the data and must be resolved along with the slip amplitude. In our test cases, we found that variations in the rupture time can trade off with the slip amplitude. All of our inversions found a distribution of rupture times that are roughly symmetric with respect to the hypocenter, i.e., a bilateral rupture. The rupture propagated slightly faster to the south than it

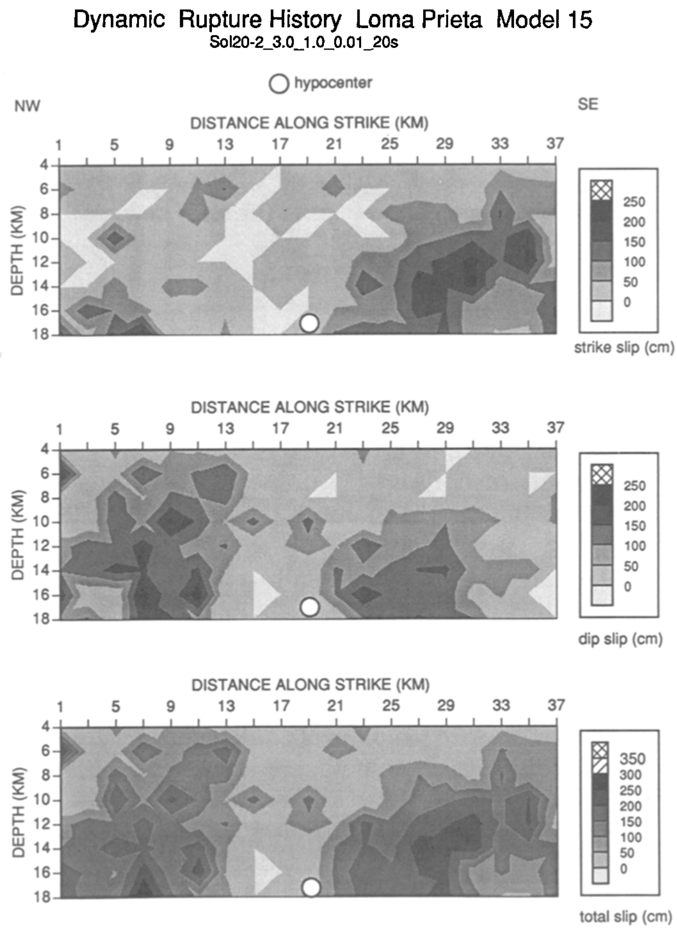

FIG. 13. Model 15: fault slip determined by inverting 40 horizontal time histories (20.0 sec) of ground velocity. Strike slip, dip slip, and total slip (cm) are contoured on the footwall. This model uses absolute timing and accounts for a foreshock that occurred 2.0 sec before the mainshock. Compare this with Figure 6a, for which the same 40 horizontal time histories (20.0 sec) were inverted.

did to the north. We found the smallest perturbations to the initial rupture time when our starting model used a velocity of 3.0 km/sec, 0.83 times the local shear-wave speed. The regions of the fault with large slip, both dip slip and strike slip, are radiating nearly simultaneously. Thus the teleseismic radiation is a mixture of strike slip and dip slip distributed nearly equally on either side of the hypocenter. Because of the bilateral rupture, the seismic radiation is complete after about 8 sec. A unilateral rupture would have produced strong ground motion for a longer duration.

The Loma Prieta earthquake has brought up an important set of questions regarding the implications for seismic hazard on the northern San Andreas. The first of these is identification of the fault on which the slip occurred. Geodetic studies indicate subsidence in the vicinity of Loma Prieta during this event, yet it is the highest peak in the Santa Cruz mountains. What slip event is lifting Loma Prieta? Was this event the characteristic rupture for the Loma Prieta segment, releasing the strain energy from the volume that encompasses the San Andreas fault in this region, or will the next earthquake occur on a deep vertical San Andreas fault? What are the implications for seismic hazard on the peninsular segment? Has it been loaded by the Loma Prieta event? Without knowledge of the pre-event stress distribution, determined by the previous event, it is difficult to make a statement regarding the state of stress or the seismic hazard at present. There are still many questions that need to be answered.

Conclusions

Slip distributions presented in this study support a rupture mechanism that contains most of the dip-slip displacement north of the hypocenter and most of the strike-slip displacement south of the hypocenter. An average rake of 115° and 156° are determined north and south of the hypocenter, respectively. The rake averaged over the entire fault plane is 137°. The average total slip is 1.5 ± 0.4 m. The rupture velocity is variable, with propagation to the south being faster than to the north. The average rupture velocity is estimated at 3.0 km/sec, approximately 0.83 times the shear-wave velocity. A rise time of 1.0 sec produces the best agreement between the synthetics and the data. The uncertainty in the method is 40 cm for strike-slip and dip-slip perturbations and 0.8 sec for rupture time perturbations. The complicated bimodal distribution of the two mechanisms of slip may suggest a more complicated fault geometry than a simple planar surface is needed. The absence of slip at shallow levels (above 8.0 km), and locally at deep levels to the north and up-dip from the hypocenter, suggests that considerable hazard may yet exist from faulting along this section of the San Andreas fault.

Acknowledgments

The authors wish to thank G. Brady and P. Mork of the USGS, and M. J. Huang, T. Q. Cao, U. R. Vetter, and A. F. Shakal of the CDMG for providing the records used in this study. We also thank David Wald and an anonymous referee for careful reviews of the manuscript. This work was supported by USGS contract 14-08-0001-G1842.

References

Aki, K. (1968). Seismic displacements near a fault, *J. Geophys. Res.* **73**, 5359–5376.

Anderson, J. G. and P. G. Richards (1975). Comparison of strong ground motion from several dislocation models, *Geophys. J. R. Astr. Soc.* **42**, 347–373.

Archuleta, R. J. (1984). A faulting model for the 1979 Imperial Valley earthquake, *J. Geophys. Res.* **89**, 4559–4585.

Archuleta, R. J. and S. M. Day (1980). Dynamic rupture in a layered medium: an example, the 1966 Parkfield earthquake, *Bull. Seism. Soc. Am.* **70**, 671–690.

Bernard, P. and R. Madariaga (1984). A new asymptotic method for the modeling of near-field accelograms, *Bull. Seism. Soc. Am.* **74**, 539–557.

Beroza, G. C. (1991). Near source modeling of the Loma Prieta earthquake: evidence for heterogeneous slip and implications for earthquake hazard, *Bull. Seism. Soc. Am.* **81**, 1603–1621.

Beroza, G. C. and P. Spudich (1988). Linearized inversion for fault rupture behavior: application to the 1984 Morgan Hill, California, earthquake, *J. Geophys. Res.* **93**, 6275–6296.

Bouchon, M. (1982). The rupture mechanism of the Coyote Lake earthquake of August 6, 1979 inferred from near field data, *Bull. Seism. Soc. Am.* **72**, 745–759.

Brune, J. N. (1970). Tectonic stress and spectra of seismic shear waves from earthquakes, *J. Geophys. Res.* **75**, 4997–5009. (1971). Correction, *J. Geophys. Res.* **76**, 5002.

CDMG (1989). Second quick report on CSMIP strong-motion records from the October 17, 1989 earthquake in the Santa Cruz Mountains, October 25, 1989.

Choy, G. L. and J. Boatwright (1990). Source characteristics of the Loma Prieta, California, earthquake of October 17, 1989 from global digital seismic data, *Geophys. Res. Lett.* **17**, 1183-1186.

Day, S. M. (1982). Three-dimensional finite difference simulation of fault dynamics: rectangular faults with fixed rupture velocity, *Bull. Seism. Soc. Am.* **72**, 1881-1902.

Dietz, L. D. and W. L. Ellsworth (1990). The October 17, 189, Loma Prieta, California, earthquake and its aftershocks: geometry of the sequence from high resolution locations, *Geophys. Res. Lett.* **17**, 1417-1420.

Hartzell, S. (1989). Comparison of seismic waveform inversion results for the rupture history of a finite fault: application to the 1986 North Palm Springs, California, earthquake, *J. Geophys. Res.* **94**, 7515-7534.

Hartzell, S. and T. Heaton (1983). Inversion of strong ground motion and teleseismic waveform data for the fault rupture history of the 1979 Imperial Valley, California, earthquake, *Bull. Seism. Soc. Am.* **73**, 1553-1583.

Hartzell, S. and T. Heaton (1986). Rupture history of the 1984 Morgan Hill, California, earthquake from the inversion of strong motion records, *Bull. Seism. Soc. Am.* **76**, 649-674.

Hartzell, S. and M. Iida (1990). Source characteristics of the 1987 Whittier Narrows, California, earthquake from the inversion of strong motion records, *J. Geophys. Res.* **95**, 12475-12486.

Hartzell, S. and C. Mendoza (1991). Application of an iterative least squares waveform inversion of strong motion and teleseismic records to the 1978 Tabas, Iran, earthquake, *Bull. Seism. Soc. Am.* **81**, 305-331.

Hartzell, S., G. S. Stewart, and C. Mendoza (1991). Comparison of L_1 and L_2 norms in a teleseismic waveform inversion for the slip history of the Loma Prieta, California, earthquake, *Bull. Seism. Soc. Am.* **81**, 1518-1539.

Heaton, T. H. and D. V. Helmberger (1979). Generalized ray models of the San Fernando earthquake, *Bull. Seism. Soc. Am.* **69**, 1311-1341.

Kanamori, H. and K. Satake (1990). Broadband study of the 1989 Loma Prieta earthquake, *Geophys. Res. Lett.* **17**, 1179-1182.

Langston, C. A., K. P. Furlong, K. S. Vogfjord, R. H. Clouser, and C. J. Ammon (1990). Analysis of teleseismic body waves radiated from the Loma Prieta earthquake, *Geophys. Res. Lett.* **17**, 1405-1408.

Lisowski, M., W. H. Prescott, J. C. Savage, and M. J. Johnston (1990). Geodetic estimate of coseismic slip during the 1989 Loma Prieta earthquake, *Geophys. Res. Lett.* **17**, 1437-1440.

Madariaga, R. (1977). High frequency radiation from crack (stress drop) models of earthquake faulting, *Geophys. J. R. Astr. Soc.* **51**, 625-651.

Maley, R., A. Acosta, F. Ellis, E. Etheredge, L. Foote, D. Johnson, R. Porcella, M. Salsman, and J. Switzer (1989). U.S. Geological Survey strong-motion records from the northern California (Loma Prieta) earthquake of October 17, 1989, *U.S. Geol. Surv. Open-File Rep. 89-568*.

Mendoza, C. and S. H. Hartzell (1989). Slip distribution of the 19 September 1985 Michoacan, Mexico, earthquake: near source and teleseismic constraints, *Bull. Seism. Soc. Am.* **79**, 655-699.

Olson, A. H. and R. Apsel (1982). Finite faults and inverse theory with applications to the 1979 Imperial Valley earthquake, *Bull. Seism. Soc. Am.* **72**, 1969-2001.

Olson, A. H., J. A. Orcutt, and G. A. Frazier (1984). The discrete wavenumber finite element method of synthetic seismograms, *Geophys. J. R. Astr. Soc.* **77**, 421-460.

Oppenheimer, D. H. (1990). Aftershock behavior of the 1989 Loma Prieta, California earthquake, *Geophys. Res. Lett.* **17**, 1199-1202.

Romanowicz, B. and H. Lyon-Caen (1990). The Loma Prieta earthquake of October 17, 1989: results of teleseismic mantle and body wave inversion, *Geophys. Res. Lett.* **17**, 1191-1194.

Scholz, C. H. (1985). The Black Mountain asperity: seismic hazard of the Southern San Francisco Peninsula, California, *Geophys. Res. Lett.* **12**, 717-719.

Spudich, P. K. P. (1980). The de Hoop-Knopoff representation theorem as a linear inverse problem, *Geophys. Res. Lett.* **7**, 717-720.

Spudich, P. and L. N. Frazer (1984). Use of ray theory to calculate high-frequency radiation from earthquake sources having spatially variable rupture velocity and stress drop, *Bull. Seism. Soc. Am.* **74**, 2061-2082.

USGS Staff (1990). The Loma Prieta, California, earthquake: an anticipated event, *Science* **247**, 286-293.

Wallace, T. C., A. Valesco, J. Zhang, and T. Lay (1991). A broadband seismological investigation of the 1989 Loma Prieta, California, earthquake: evidence for deep slow slip?, *Bull. Seism. Soc. Am.* **81**, 1622-1646.

Wald, D., D. V. Helmberger, and T. H. Heaton (1991). Rupture model of the 1989 Loma Prieta earthquake from the inversion of strong motion and broadband teleseismic data *Bull. Seism. Soc. Am.* **81**, 1540-1572.

Zhang, J. and T. Lay (1990). Source parameters of the 1989 Loma Prieta earthquake determined from long-period Rayleigh waves, *Geophys. Res. Lett.* **17**, 1195-1198.

Department of Geological Sciences
and Institute for Crustal Studies
University of California at Santa Barbara
Santa Barbara, California 93106
(J.H.S., R.J.A.)

U.S. Geological Survey
MS 966
Box 25046
Denver Federal Center
Denver, Colorado 80225
(S.H.H.)

Manuscript received 5 January 1991